Advanced Healthcare Materials

ADVANCED HEALTHCARE MATERIALS
www.advhealthmat.de

RESEARCH ARTICLE

High-Entropy Metal–Organic Cages as Multienzyme Mimetics for the Mitigation of Acute Kidney Injury

Demei Sun[1,2] | Xuesong Feng[2] | Qing Miao[1,2] | Xinyuan Zhu[1] | Jinghui Yang[3] | Youfu Wang[1]

[1]School of Chemistry and Chemical Engineering, State Key Laboratory of Polyolefins and Catalysis, Shanghai Jiao Tong University, Shanghai, P. R. China | [2]School of Pharmacy, China Medical University, Shenyang, P. R. China | [3]Department of Organ Transplantation, Shanghai Changzheng Hospital, Naval Medical University, Shanghai, P. R. China

Correspondence: Jinghui Yang (yjh@smmu.edu.cn) | Youfu Wang (wyfown@sjtu.edu.cn)

Received: 23 September 2025 | **Revised:** 25 November 2025 | **Accepted:** 11 December 2025

Keywords: acute kidney injury | high-entropy | isostructural substitution | metal–organic cage | multienzyme mimetics

ABSTRACT

Precise morphological and compositional regulation of high-entropy nanoparticles (HENPs) represents a fundamental prerequisite for advancing their applications in catalysis and electronics. Conventional synthesis approaches, however, face challenges stemming from intrinsic elemental segregation dynamics and the unpredictable atomic configurations within individual nanoparticles. To address this, we introduce an isostructural substitution strategy for constructing HENPs, utilizing predefined molecular scaffolds to guide multielemental integration. By employing a calixarene-based octahedral metal–organic cage (MOC) featuring six well-defined M_4O clusters (totaling 24 metal sites) as a structural template, we systematically incorporate five distinct metallic elements (Mg, Mn, Co, Ni, Zn) through solvothermal synthesis, yielding high-entropy MOC (HEMOC) nanoobjects in gram scale. These engineered HEMOCs preserve the octahedral skeleton and structural uniformity, maintain readily accessible catalytic centers with tunable stoichiometry, and exhibit exceptional aqueous-phase stability. Significantly, the diverse heterometallic M_4O clusters within HEMOCs function as cluster nanozymes, demonstrating amplified multienzyme-mimetic catalytic activity for scavenging reactive oxygen species. Demonstrating favorable biocompatibility profiles in biological evaluations, the optimized HEMOCs successfully attenuate inflammation in acute kidney injury models, suggesting therapeutic potential for oxidative stress-associated pathologies.

1 | Introduction

High-entropy nanoparticles (HENPs), defined as nanoscale solid-solution structures integrating five or more principal elements in near-equimolar ratios, represent a paradigm shift in materials science [1–3]. Their vast elemental combinations and diverse spatial distributions enable unique multicomponent interactions and novel physicochemical properties, garnering significant attention for applications in catalysis, energy storage, and biomedicine [4–6]. Crucially, HENPs can optimize the electronic structures and surface reactivities of metallic sites near-continuously, overcoming the limitation of traditional catalysts constrained by linear scaling relations [7, 8]. This is achieved by tunably managing adsorption/desorption energies of reaction intermediates through inherent high entropy, unexpected synergies, strong lattice distortions, and slow atomic diffusion [9–11]. However, HENP development faces fundamental challenges: (i) Synthetic control: Elemental immiscibility and physicochemical disparities (e.g., atomic radius, reduction potentials) hinder homogeneous mixing, often causing phase segregation under near-equilibrium conditions [12, 13]. Nonequilibrium techniques (e.g., thermal shock, cryomilling) kinetically trap metastable phases but lack

Demei Sun and Xuesong Feng contributed equally to this work as co-first authors.

precision in size, morphology, and surface topology. Harsh conditions also cause an uncontrollable number of atoms per particle, limiting structural control [14–16]. (ii) Structural complexity: Random atomic arrangements obscure active sites and structure-property relationships. Rational design within the vast compositional space (>10^6 combinations) relies heavily on data-driven approaches; high-throughput screening and machine learning cover <1% of possibilities, while theoretical models oversimplify surface interactions [17–19]. (iii) Characterization limits: Conventional techniques cannot resolve multielemental synergy atomically. Advanced characterization modalities, including atomic electron tomography (AET) and X-ray absorption spectroscopy (XAS), remain indispensable for material analysis, yet these techniques inherently aggregate compositional data based on atomic number, potentially obscuring element-specific functionalities in complex systems [20, 21].

To overcome these challenges, particularly inadequate control over dimensional parameters and structural topology, we propose an isostructural substitution strategy to fabricate HENPs using predefined molecular scaffolds that guide multielemental integration [22–24]. This approach enables the systematic integration of multiple metallic constituents into atomically defined nanoarchitectures with predetermined metallic sites and spatial arrangements, ensuring monodisperse HENP dimensions and structural homogeneity. Metal–organic cages (MOCs) are ideal platforms due to their atomically precise architectures, discrete coordination sites, tunable ligand fields, and intrinsic stability [25–28]. The strategic substitution of multiple metallic species within isostructural MOC matrices—preserving topological equivalence while altering elemental composition—ensures reproducible elemental distribution, stoichiometric precision, and site-resolved metal deposition. Crucially, this methodology circumvents thermodynamic limitations through confinement within programmed coordination spaces, enforcing heterometallic integration even among elements exhibiting pronounced immiscibility. This atomic-level control addresses critical limitations in conventional HENP fabrication: ill-defined atomic configurations, compositional batch-to-batch variations, and surface chemical heterogeneities that hinder precise structure-performance correlation.

Expanding upon this foundation, we demonstrate the construction of high-entropy MOCs (HEMOCs) through template-directed synthesis using calixarene-based octahedral templates. Each cage contains 24 identical metal sites organized into six M_4O clusters. While prior studies incorporated single metals (e.g., Mg, Mn, Fe, Co, Ni, Zn) or bimetallic systems (e.g., Co/Ni) [29–32], we now construct HEMOCs via isostructural substitution of five distinct metallic elements (Mg, Mn, Co, Ni, Zn) in gram scale using controlled solvothermal synthesis (Figure 1). This advancement achieves atomic-level integration of high-entropy materials, yielding five critical attributes: (i) Predetermined topological structure and atomic number; (ii) Uniformly ultrasmall architectures (<10 nm) with atomic-level homogeneity; (iii) Stoichiometric control maximizing configurational entropy; (iv) Readily accessible catalytic centers and inherent cavities for synergistic catalysis; (v) Stability in physiological environments. Due to the emergent synergistic properties from HENPs surpassing those of monometallic or phase-separated counterparts, diverse heterometallic M_4O clusters enable HEMOCs to function as cluster nanozymes with enhanced multi-enzymatic activity (superoxide dismutase (SOD)/catalase (CAT)/glutathione peroxidase (GPx)) that suggests therapeutic potential against oxidative stress-related pathologies [33–36]. Computational studies validate that heterometallic clusters (e.g., MgMnCoNiO) optimize radical adsorption energies and lower reaction barriers. This approach resolves persistent challenges in HENP fabrication while establishing a versatile paradigm for engineering entropy-driven nanomaterials with programmable biofunctionality.

2 | Results and Discussion

2.1 | Synthesis and Characterization of HEMOC

The five metals were selected based on their complementary redox properties (Mn, Co, Ni for redox catalysis) [29], structural role (Mg, Zn for stability and electronic modulation), and their ability to form stable M_4O clusters within the calixarene-based MOC skeleton [37]. To verify the feasibility of isostructural substitution in calixarene-based octahedral MOCs, we systematically prepared a series of MOCs containing unary, binary, trinary, quaternary, and quinary metal compositions (designated as MOC-U, MOC-B, MOC-T, MOC-Qua, and MOC-Q, respectively) through a one-pot solvothermal method. The synthesis employed equimolar ratios of metal chloride precursors ($MgCl_2{\cdot}6H_2O$, $MnCl_2{\cdot}4H_2O$, $CoCl_2{\cdot}6H_2O$, $NiCl_2{\cdot}6H_2O$, and $ZnCl_2$) with 4-*tert*-butylsulfonylcalix[4]arene (SC4A) and benzene-1,3,5-tricarboxylic acid (H_3BTC) as organic linkers. Detailed synthetic procedures can be found in the experimental section. All products crystallized as highly crystalline cubic microcrystals (Figure S1), with powder X-ray diffraction (PXRD) patterns confirming their isostructural nature, indicating the practicability of the isostructural substitution strategy (Figure S2). Building upon these results, we synthesized a series of MOC-Q variants (MOC-Q1∼9) with systematically varied metal ratios by adjusting the precursor input ratios. Inductively coupled plasma mass spectrometry (ICP-MS) analysis revealed a strong correlation between input ratios and final metal compositions (Table S1). Notably, we observed an inverse relationship between Zn incorporation and Ni/Co content, likely attributable to Zn's larger atomic radius and weaker occupancy capability. By means of systematic optimization, MOC-Q9 with ΔS_{conf} = 1.51R was identified to demonstrate pronounced high-entropy characteristics, leading to its designation as HEMOC (Figure 2a). Owing to the simplicity of the solvothermal method, gram-scale HEMOC was readily prepared by increasing the precursor loading.

The PXRD plot of HEMOC consisting with the simulated plot from the corresponding single crystal, confirmed the formation of the expected octahedral MOC [29]. As a result, HEMOC adopts an octahedral geometry with the molecular formula $[(M_4O)_6(SC4A)_6(BTC)_8]$ (M = Mg/Mn/Co/Ni/Zn) (Figure 2b). To corroborate the structural configuration of HEMOC, single-crystal analysis was pursued based on its exceptional crystallinity. X-ray diffraction data demonstrate that HEMOC adopts the tetragonal *I*4/m space group, maintaining structural congruence with MOC-U analogues (Figure S3). There exist four crystallographically independent metal sites, each being six-coordinated by two phenoxy μ_2-O atoms and one axial sulfonyl oxygen atom from calixarene, two carboxyl oxygen atoms from dis-

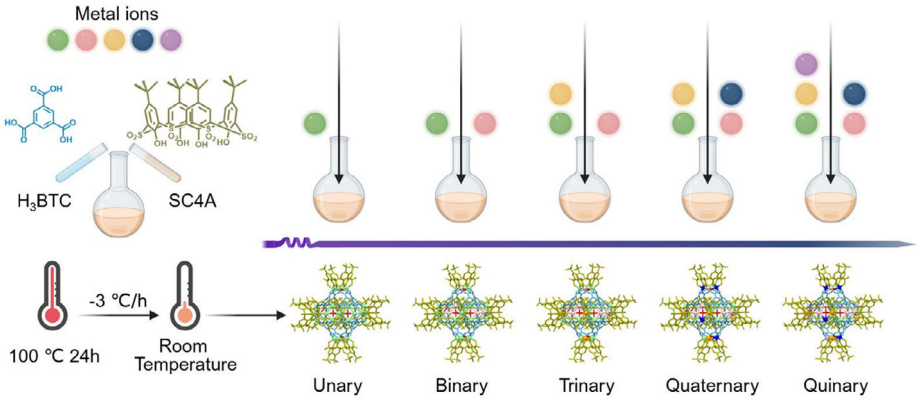

FIGURE 1 | Construction of multi-metallic MOCs through isostructural substitution in calixarene-based octahedral MOCs. Created with www.biorender.com.

tinct H_3BTC ligands, and one μ_4-O atom. The uncertainty of element types on metal sites confirms successful isostructural substitution of all five metal ions. Fourier-transform infrared (FTIR) spectroscopy further validated HEMOC formation, showing characteristic stretching vibration from SC4A (2960 cm^{-1}, C-H stretch), while the absence of carbonyl stretching vibration from H_3BTC at ~1600 cm^{-1} confirmed the integration of these building blocks (Figure S4). Due to the discrete molecular nature, the molecular weights determination by matrix-assisted laser desorption/ionization time-of-flight (MALDI-TOF) mass spectrometry yielded values between 7406.812 Da (MOC-Mg) and 8360.169 Da (MOC-Zn) for MOC-Us, consistent with the calculated values, with HEMOC exhibiting a multimodal distribution within this range (Figure 2c; Figure S5), confirming molecular-level metal mixing. Morphological characterization by scanning electron microscopy (SEM) revealed well-defined cubic crystals (~50 μm) with sharp edges (Figure 2d). Energy-dispersive X-ray spectroscopy (EDS) mapping demonstrated homogeneous elemental distribution in HEMOC, contrasting with the phase-separated elemental distribution observed in physical mixtures of five MOC-Us (Figure S6). Quantitative EDS analysis yielded metal ratios consistent with ICP-MS data, satisfying the strict criteria for high-entropy materials. These comprehensive characterization results unambiguously confirm the successful synthesis of a HEMOC with atomic-level metal mixing.

To further corroborate the atomic-level integration of Mg, Mn, Co, Ni, and Zn in HEMOC, we conducted comprehensive X-ray photoelectron spectroscopy (XPS) analysis (Figure 2e; Figures S7 and S8). The technique provides crucial insights into elemental interactions, oxidation states, and surface molecular structure through careful examination of peak positions and spectral features. The high-resolution spectra revealed distinct electronic environments for each metal component: Mg 1s exhibited a characteristic peak at 1304.2 eV, corresponding to magnesium oxides; Mn 2p spectrum displayed spin-orbit doublets at 653.6 (2p1/2) and 641.7 eV (2p3/2) with associated satellite peaks; Co 2p region showed signatures at 797.4 (2p1/2) and 781.3 eV (2p3/2), with deconvolution indicating the coexistence of Co^{2+} and Co^{3+} species; Ni 2p peaks at 873.7 (2p1/2) and 856.3 eV (2p3/2) confirmed metallic character; Zn 2p doublets appeared at 1045.4 (2p1/2) and 1022.2 eV (2p3/2). Notably, the elemental composition (C: 66.34%, O: 24.18%, S: 4.47%, metals: 5%) matched precisely with the expected octahedral MOC structure. Comparative analysis between HEMOC and respective MOC-Us revealed subtle but significant binding energy shifts (e.g., Mg 2p at 50.09 eV in HEMOC vs 50.16 eV in MOC-Mg), demonstrating modified coordination environments arising from heterometallic interactions in the high-entropy system.

The uniform, nanoscale architecture of HEMOC enables excellent solubility in diverse solvents, including N,N-dimethylformamide (DMF), methylene chloride (DCM), chloroform, and dimethyl sulfoxide (DMSO). Remarkably, HEMOC exhibits outstanding colloidal and structural stability under physiological conditions. It maintained its colloidal integrity in water, phosphate buffered saline (PBS), and fetal bovine serum (FBS) for over 5 days, with a consistent hydrodynamic diameter of 7.6 nm (PDI ~0.21) and a zeta potential of −26 mV (Figures S9 and S10); concurrently, ICP-MS analysis revealed negligible metal release (< 0.1%) after the same period, further confirming its robustness. UV–vis characterization showed distinct absorption maxima at 275 and 355 nm (Figure S11), well-separated from relevant analytical wavelengths for subsequent enzymatic studies. This combination of advanced spectroscopic characterization and solution behavior studies provides compelling evidence for the successful creation of a well-mixed, high-entropy coordination system with exceptional structural integrity and solution processability.

2.2 | Multienzyme Mimetic Activities of HEMOC

Capitalizing on its unique structural features and accessible cavity with discrete heterometallic sites, HEMOC demonstrates remarkable potential as cluster-based multienzyme mimetics [36]. Our comprehensive evaluation revealed its superior antioxidant enzyme-mimicking activities, including superoxide dismutase (SOD), catalase (CAT), and glutathione peroxidase (GPx) functionalities, outperforming both MOC-U analogues and their physical mixture (MOC-PM).

2.2.1 | SOD-Like Activity

Using two distinct analytical approaches, we systematically evaluated the SOD-like performance. The Nitro blue tetrazolium (NBT) can be specifically reduced by superoxide anion ($\bullet O_2^-$)

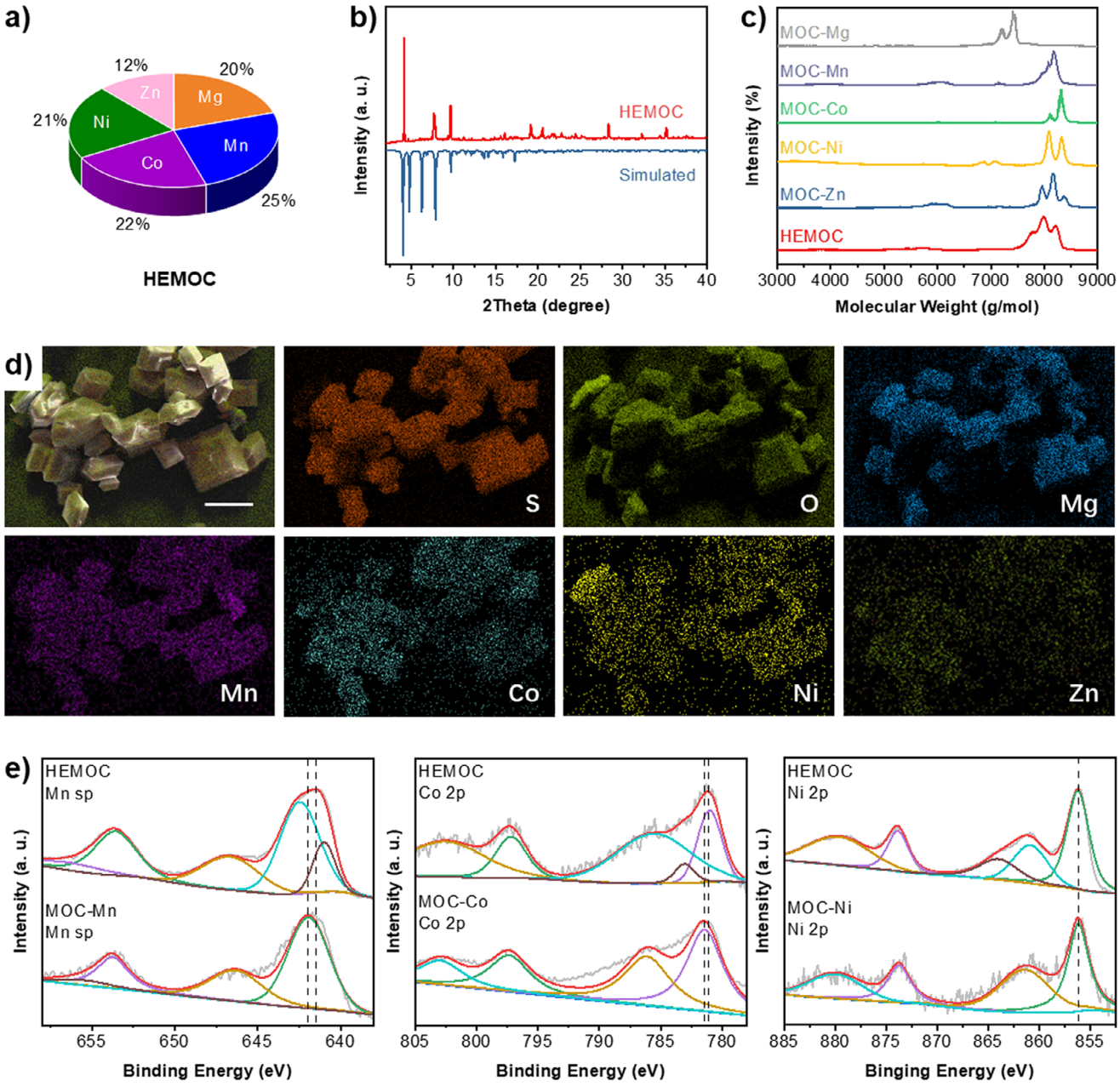

FIGURE 2 | Systematic structural investigation of HEMOC. (a) Elemental stoichiometry determination via ICP-MS. (b) Comparative analysis of experimental PXRD profiles and MOC-U simulations. (c) MALDI-TOF mass spectra demonstrating molecular weight distributions of HEMOC and corresponding MOC-Us. (d) SEM morphological analysis coupled with EDS spatial distribution mapping, scale bar = 50 μm. (e) High-resolution XPS spectra of metallic coordination environments in HEMOC versus MOC-Us.

from riboflavin and L-methionine under light to produce blue methylhydrazone as an indicator with characteristic absorption at 560 nm. The lowest absorption demonstrated HEMOC's exceptional $\bullet O_2^-$ scavenging capability (Figure 3a; Figure S12). Complementary studies employing KO_2/18-Crown-6 systems with monoformazan as an indicator at 680 nm revealed a concentration-dependent inhibitory effect, yielding a specific activity of 8.45 U/mg (Figure S13) [38]. Electron paramagnetic resonance (EPR) spectroscopy with 5,5-dimethyl-1-pyrroline N-oxide (DMPO) trapping provided direct evidence of $\bullet O_2^-$ elimination, showing dramatic signal reduction upon HEMOC treatment (Figure 3b).

2.2.2 | CAT-Like Performance

HEMOC exhibited outstanding H_2O_2 decomposition activity compared with MOC-Us and MOC-PM, as quantified by dissolved oxygen measurements. The catalytic efficiency showed positive correlations with both reaction time and H_2O_2 concentration (Figure 3c; Figure S14). Kinetic analysis revealed favorable Michaelis-Menten parameters (K_M = 2.7 mM, V_{max} = 20 mg/L/min), higher than most of the non-noble metallic catalysts, indicating efficient oxygen generation (Figure 3d). Notably, 3,3',5,5'-tetramethylbenzidine (TMB) oxidation studies and EPR spectroscopy revealed HEMOC's selective preference

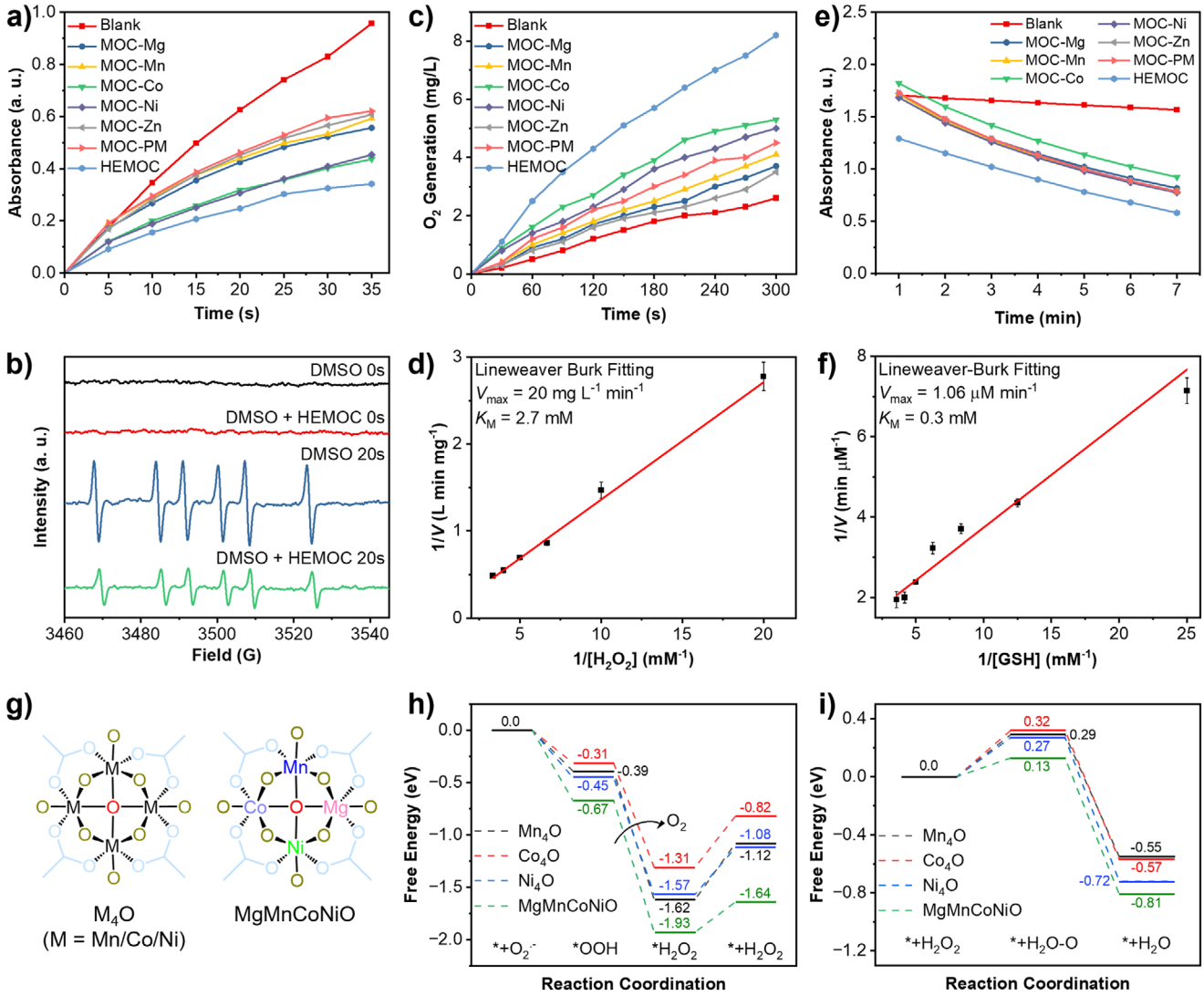

FIGURE 3 | Systematic evaluation of HEMOC's multienzyme-mimetic functionalities. (a) Spectrophotometric quantification of SOD-mimetic efficacy. (b) EPR spectral confirmation of SOD-mimetic behavior. (c) Oxygen evolution quantification for CAT-mimetic performance assessment. (d) Kinetic parameter determination of CAT-mimetic enzymatic processes. (e) GSH depletion monitoring via UV–vis spectroscopy for GPx-mimetic capacity. (f) Comparative kinetic analysis of GPx-mimetic catalytic efficiency. (g) Structural representation of MOC-U versus HEMOC active sites. DFT- derived energy landscapes for h) SOD-mimetic pathways and (i) for CAT-mimetic pathways.

for $H_2O_2 \rightarrow O_2$ conversion over •OH generation, distinguishing it from monometallic counterparts (Figure S15).

2.2.3 | GPx-Like Function

The 5,5'-dithio-bis-(2-nitrobenzoic acid) (DTNB)-based assay with characteristic absorption at 412 nm confirmed HEMOC's ability to catalyze glutathione (GSH) oxidation, with activity enhancement at higher nanozyme concentrations (Figure 3e; Figure S16). The Kinetic studies demonstrated excellent substrate affinity (K_M = 0.3 mM for GSH) and reaction velocity (V_{max} = 1.06 μM/min) (Figure 3f).

Given the remarkable multifunctional enzyme-like activities, we employ theoretical investigations into the active M_4O clusters to elucidate the origin of HEMOC's enhanced performance. Due to the low abundance and lack of significant redox activity of Zn, the MgMnCoNiO cluster was selected as a representative cluster in HEMOC for theoretical calculations (Figure 3g). For SOD-like activity, the heterometallic MgMnCoNiO cluster showed superior •OOH adsorption (−0.67 vs −0.31 to −0.45 eV for monometallic clusters) (Figure 3h). In CAT-like processes, it exhibited the lowest activation barrier (0.13 vs 0.27 to 0.32 eV) for H_2O_2 decomposition (Figure 3i) [31]. These computational findings, supported by detailed reaction pathway analysis (Figures S17 and S18), rationalize the experimental observations of enhanced catalytic efficiency.

The convergence of multienzyme-mimetic cascade capabilities, combined with systematic interrogation of heterometallic cooperativity, establishes HEMOC as a viable antioxidant nanoplatform [39]. Its ability to simultaneously address various ROS through distinct yet complementary mechanisms suggests broad potential in oxidative stress management applications [40]. It is worth mentioning that the enhanced activity likely arises from both the

diversity of active sites and the specific synergistic interactions among metals (e.g., Mn-Co-Ni), rather than entropy alone.

2.3 | In Vitro Cellular Protective Capacity and ROS-Scavenging Efficacy of HEMOC

Given the enhanced multienzyme-mimetic performance of HEMOC relative to monometallic counterparts, the biological implications of these catalytic enhancements were systematically investigated using HK-2 human renal proximal tubular epithelial cells. Biocompatibility was evaluated through methylthiazolyldiphenyl-tetrazolium (MTT) cytotoxicity assays and erythrocyte membrane integrity assessments. The results demonstrated that cellular viability remained above 90% at a concentration of 30 μg/mL and was maintained at approximately 80% at the higher concentration of 300 μg/mL across all MOC groups (Figure 4a). Hemocompatibility analysis demonstrated favorable profiles (<5% hemolysis) at 300 μg/mL concentration (Figure 4b). Cellular internalization capacity was confirmed via ICP-MS, quantifying approximately 27 μg of internalized material per million HK-2 cells (Figure S19).

We next investigated the protective effects of MOCs against hypoxia/reoxygenation (H/R)-induced oxidative damage. Intracellular ROS levels were assessed using the fluorescent probe 2,7-dichlorodihydrofluorescein diacetate (DCFH-DA) (Figure 4c). H/R treatment was associated with marked ROS accumulation, as indicated by enhanced green fluorescence intensity. Notably, MOC administration resulted in reduced ROS generation, with HEMOC exhibiting the most pronounced antioxidant effect. These findings were corroborated by flow cytometry analysis, which demonstrated significantly decreased intracellular ROS levels in HEMOC-treated cells relative to other MOC-U groups (Figure 4d). Further evaluation via MTT assays indicated that HEMOC treatment markedly enhanced cell viability following H/R-induced injury (Figure 4e).

Mitochondria are central organelles in cellular bioenergetics and redox homeostasis, yet demonstrate particular susceptibility to ROS-mediated oxidative impairment [41]. To evaluate mitochondrial protection, JC-1 staining was utilized to determine mitochondrial membrane potential dynamics (Figure 4f) [42]. Mitochondria with preserved membrane polarization accumulate JC-1 aggregates exhibiting red fluorescence, whereas depolarized counterparts display green fluorescence associated with JC-1 monomeric forms. Notably, HEMOC treatment elevated the red fluorescence ratio by 42.7% compared to untreated controls, indicating enhanced maintenance of mitochondrial transmembrane polarity (Figure 4g). These findings collectively establish that HEMOC confers cytoprotection through dual mechanisms involving ROS neutralization and mitochondrial functional preservation, suggesting therapeutic applicability in renal pathologies characterized by oxidative stress.

2.4 | In Vivo Protective Efficacy of HEMOC Against Renal Ischemia/Reperfusion (I/R) Injury

To establish the biosafety profile, we first conducted acute toxicity studies by administering MOCs intravenously at twice the therapeutic concentration (300 μg/ml, 0.4 mL). Histopathological evaluation of major organs through hematoxylin and eosin (H&E) staining at 48 h post-administration revealed no detectable pathological alterations across experimental groups (Figure S20), suggesting favorable in vivo biocompatibility at supratherapeutic doses. A murine model of renal I/R injury was established, with the detailed experimental timeline illustrated in the schematic diagram (Figure 5a). Renal functional assessment in I/R-injured mice demonstrated peak serum creatinine concentrations at 24 h post-injury. While MOC-Us induced moderate creatinine diminution, HEMOC administration yielded significantly reduced concentrations (Figure 5b). Histomorphological evaluations aligned with functional measurements, with HEMOC-treated specimens displaying preserved tubular architecture, attenuated brush border erosion, diminished intratubular cast formation, and ameliorated glomerular congestion compared to MOC-U groups (Figure 5c,d).

Dihydroethidium (DHE) fluorescent imaging revealed substantial ROS accumulation in I/R-damaged renal tissue, as indicated by elevated fluorescence intensity (Figure 5e). This oxidative stress was significantly attenuated by MOCs treatments, with HEMOC exhibiting the most pronounced reduction (Figure 5h). Immunofluorescence analysis of renal injury biomarkers revealed that HEMOC pretreatment effectively reduced I/R-induced overexpression of NGAL and KIM-1 by 59% and 67%, respectively (Figure 5f,i). Terminal deoxynucleotidyl transferase dUTP nick-end labeling (TUNEL) assays further identified significantly diminished apoptotic cell populations in HEMOC-treated cohorts compared to I/R controls (Figure 5g,j), indicating combinatorial antioxidant and antiapoptotic mechanisms underlying renal protection.

3 | Conclusions

In summary, this study presents an innovative paradigm for designing high-entropy nanomaterials through isostructural substitution in atomically precise nanoobjects, successfully bridging the gap between atomic precision and multimetallic complexity. By leveraging the well-defined coordination environment of calixarene-based MOCs, we developed HEMOCs that overcome fundamental limitations of conventional high-entropy materials while exhibiting unprecedented structural uniformity and atomic-level homogeneity. The entropy-stabilized heterometallic clusters in HEMOCs demonstrate synergistic multienzyme mimetics with enhanced triple-enzyme mimetic activities, offering superior ROS scavenging capabilities validated by both experimental and computational studies. Beyond their remarkable catalytic performance, HEMOCs show excellent biocompatibility and therapeutic potential, as evidenced by their significant protective effects against oxidative stress-related tissue damage. This work establishes a generalizable platform for engineering high-entropy materials with atomic precision, opening new avenues for exploring the vast compositional space of multimetallic systems. The demonstrated strategy contributes to fundamental understandings of high-entropy material behavior while demonstrating translational potential for developing tailored multifunctional nanomaterials in biomedical and catalytic applications requiring precise multimetallic coordination control.

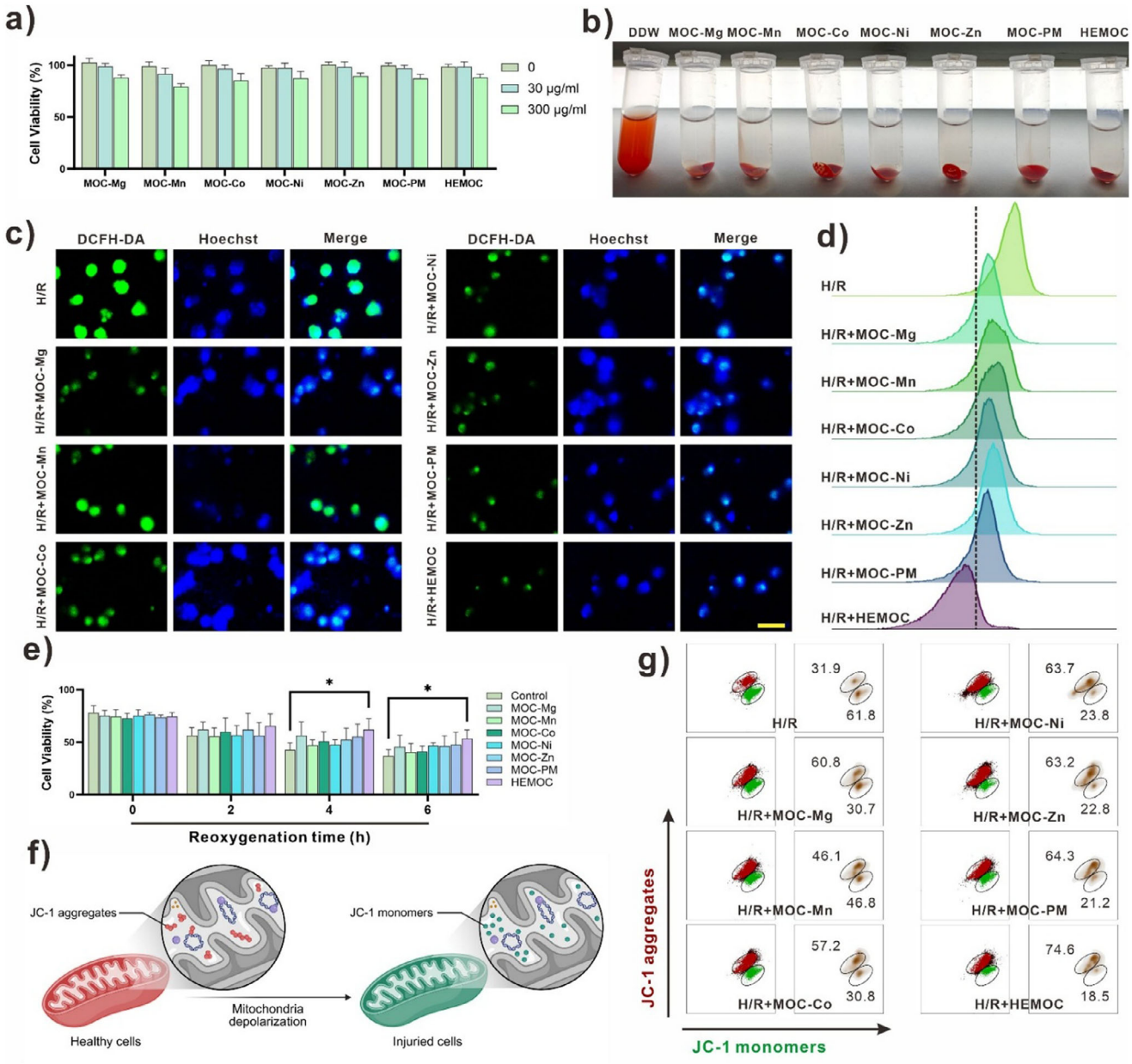

FIGURE 4 | In vitro assessment of HEMOC's cytoprotective efficacy and antioxidant capacity. (a) Cytotoxicity assays of MOCs on HK-2 cells were determined by MTT assay ($n = 3$). (b) Hemocompatibility profile quantifying erythrocyte membrane integrity through comparative hemolytic response analysis. DDW: Double-distilled water. (c) Confocal fluorescence micrographs visualizing ROS-mediated oxidative stress (DCFH-DA, green) with nuclei counterstained using Hoechst 33342, scale bars = 20 μm. (d) Flow cytometric quantification of intracellular ROS accumulation in MOC-treated HK-2 cells. (e) Protective effects of MOCs against H/R-induced cytotoxicity measured by MTT assay ($n = 3$). (f) Schematic representation of molecular mechanisms underlying JC-1 probe-based dual-emission monitoring of mitochondrial polarization states. Created with www.biorender.com. (g) Flow cytometric quantification of JC-1 fluorescence ratio (red/green) as indicators of mitochondrial transmembrane potential. Data are presented as mean ± s.d. * $p < 0.05$.

4 | Experimental Section

4.1 | Materials

All chemicals and solvents were commercially available and used without further purification. Double-distilled water (DDW) was used in the preparation of aqueous solutions. $MgCl_2{\cdot}4H_2O$, $MnCl_2{\cdot}4H_2O$, $CoCl_2{\cdot}6H_2O$, $NiCl_2{\cdot}6H_2O$, $ZnCl_2$, N,N-dimethylformamide (DMF), methanol (MeOH), and dimethyl sulfoxide (DMSO) were purchased from Shanghai Titan Scientific Co., Ltd. (China). Benzene-1,3,5-tricarboxylic acid (H_3BTC) was purchased from Bide Pharmatech Co., Ltd. (China). H_2O_2 was purchased from Sinopharm Chemical Reagent Co., Ltd. (China). 4-*tert*-Butylsulfonylcalix[4]arene (SC4A) was synthesized according to previous reports. MTT cell proliferation and cytotoxicity assay kit (C0009S) and reactive oxygen species detection kit (S0033S) were purchased from Beyotime Biotech. Inc.

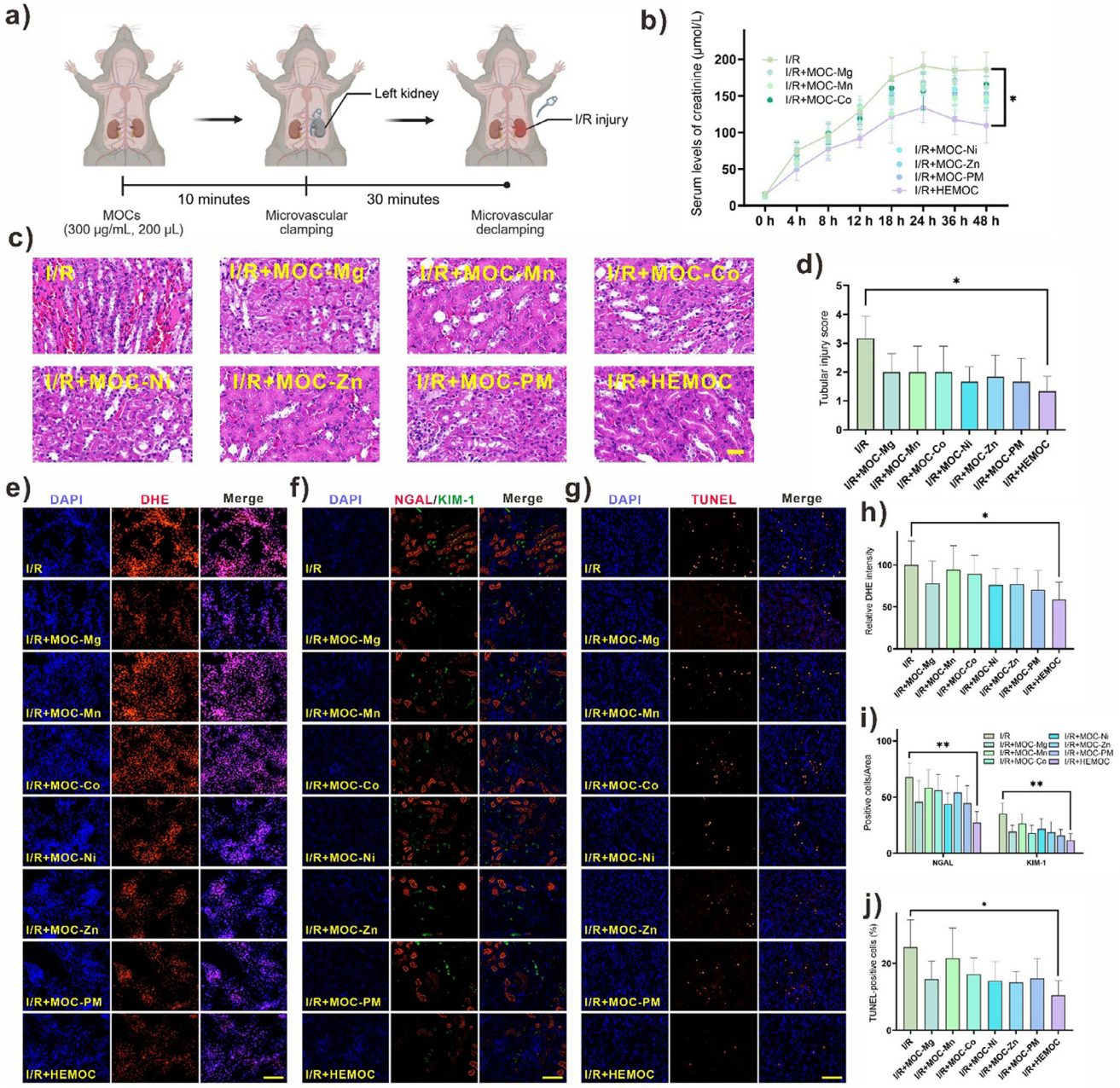

FIGURE 5 | In vivo renoprotective effects of HEMOC against renal I/R injury. (a) Renal I/R model and drug administration protocol. Created with www.biorender.com. (b) Temporal profiles of serum creatinine levels following renal I/R injury ($n = 4$). (c) Representative H&E-stained kidney sections (40× magnification) at 24 h post-reperfusion, scale bar = 100 μm. (d) Quantitative assessment of tubular injury severity based on standardized scoring criteria. (e) Representative immunofluorescence images of DHE staining, scale bars=100 μm. (f) Representative immunofluorescence images showing NGAL and KIM-1 expression, scale bars = 100 μm. (g) Representative immunofluorescence of TUNEL-stained kidney sections, scale bars=100 μm. (h) Quantitative analysis of relative DHE fluorescence intensity ($n = 6$). (i) The count of the NGAL/KIM-1 positive cells ($n = 6$). (j) The count of the TUNEL-positive cells ($n = 6$). Data are presented as mean±s.d. * $p < 0.05$, ** $p < 0.01$.

4.2 | Instrumentation

Powder X-ray diffraction (PXRD) spectra were conducted on an X-ray diffractometer (D8 Advance). Single-crystal XRD data were gathered with a Bruker D8 Venture diffractometer, maintaining the crystal at 100–173 K. Mass spectrums were measured using a matrix-assisted laser desorption/ionization time of flight (MALDI-TOF) mass spectrometry (Bruker). The Fourier transform infrared (FT-IR) spectrum was collected using a FT-IR spectrometer with an attenuated total refraction attachment (Nicolet iS50). The binding energies of the elements were analyzed using an X-ray photoelectron spectroscopy (XPS) (ESXCALAB Xi+) instrument from Thermo Scientific and the C1s peak at 284.8 eV. Inductively coupled plasma mass spectrometry (ICP-MS) (i CAP Q, Thermo) was used to detect element amount and cellular uptake. Morphology images and element distribution were recorded on an Apreo 2S field emission scanning electron microscope (SEM) at 15 kV acceleration voltage. The enzyme

activities were assessed using a UV-2600i UV–vis spectrometer (Shimadzu), an electron paramagnetic resonance (EPR) spectroscopy (Bruker EMXplus), and a dissolved oxygen meter.

4.3 | Synthesis of HEMOC

HEMOC contains five metallic elements, which were synthesized using solvtheraml method. A glass vial containing $MgCl_2{\cdot}4H_2O$, $MnCl_2{\cdot}4H_2O$, $CoCl_2{\cdot}6H_2O$, $NiCl_2{\cdot}6H_2O$, and $ZnCl_2$ (sum of 0.05 mmol), SC4A (0.01 mmol), H_3BTC (0.03 mmol), DMF (1.0 mL), and methanol (50 μL) was sealed and heated at 100°C for 24 h. After cooling to room temperature at a rate of 3°C/min, cubic crystals were obtained and subsequently dried under vacuum. The input molar ratios of metallic precursors are listed in Table S1. MOCs with unary, binary, trinary, quaternary, and quinary metallic types were constructed in the same procedure, and the input molar amounts of different metals or metallic ratios in a MOC were the same, with 0.05 mmol in total.

4.4 | Synthesis of HEMOC in Gram Scale

A glass vial containing $MgCl_2{\cdot}4H_2O$, $MnCl_2{\cdot}4H_2O$, $CoCl_2{\cdot}6H_2O$, $NiCl_2{\cdot}6H_2O$, and $ZnCl_2$ (sum of 0.75 mmol), SC4A (0.15 mmol), H_3BTC (0.45 mmol), DMF (15.0 mL), and methanol (0.75 mL) was sealed and heated at 100°C for 24 h. After cooling at −3°C/min to room temperature, cubic crystals can be observed through centrifugation and dried under vacuum (1.20 g).

4.5 | Detection of SOD-Like Activity

The superoxide dismutase (SOD) activities of HEMOC were measured using a sensitive $\bullet O_2^-$ probe-NBT, by measuring the inhibition of HEMOC on the reduction of NBT under light conditions. The characteristic absorption peak was observed at 560 nm. Typically, HEMOC (1 mg/mL, 50 μL), NBT (0.75 mM, 250 μL), riboflavin (0.02 mM, 250 μL), Met (130 mM, 250 μL), EDTA-Na_2 (0.1 mM, 250 μL) were mixed in phosphate buffer (pH = 7.4, 50 mM, 2 mL) under a constant intensity UV lamp, and the changes in absorbance value at 560 nm were measured at intervals of 5 s. In addition, to reduce the influence of light and poor water solubility of NBT on the experimental results, we also used KO_2 as a source of $\bullet O_2^-$ and replaced the solvent with DMSO. If there was an excess of NBT in the reaction system (n_{KO2}: n_{NBT}<1), only monoformazan was formed with a maximum absorption peak appearing at about 680 nm. In a typical experiment, 18-Crown-6 (enhances the dissolution of KO_2 in DMSO), NBT, and HEMOC were added to DMSO, and observed the absorbance of monoformazan at 680 nm. The $\bullet O_2^-$ inhibition rate was evaluated through changing the concentration of HEMOC in the reaction system (final concentration of 0–120 μg/mL). Each experiment was conducted three times to minimize experimental error. Furthermore, $\bullet O_2^-$ was measured by EPR at room temperature. The sample had a final concentration of riboflavin (4.3 μM), Met (27.8 mM), EDTA-Na_2 (0.02 mM), DMPO (3 mg/mL), HEMOC (0.2 mg/mL), or isovolumetric DMSO in phosphate buffer (50 mM).

4.6 | Detection of CAT-Like Activity

The catalase (CAT) activity assays of HEMOC were conducted at room temperature by measuring the oxygen produced with a portable oxygen detector. Typically, H_2O_2 (0.4 M, 60 μL) and HEMOC (1 mg/mL, 10 μL) were added to phosphate buffer (pH = 7.2) to make a total volume of 15 mL. The generated oxygen solubility (unit: mg/L) was recorded from 0 to 5 min. In addition, the effect of H_2O_2 concentration on the catalytic effect was also studied. It was performed by adding different concentrations of H_2O_2 (0, 0.05, 0.10, 0.15, 0.20, 0.25, 0.30 mM).

4.7 | Detection of GPx-Like Activity

5,5'-Dithiobis(2-nitrobenzoic acid) (DTNB) was employed in accessing the glutathione peroxidase (GPx)- mimicking activity of MOCs. Glutathione (GSH) (1 mM, 80 μL), H_2O_2 (0.4 M, 20 μL), and MOCs nanozyme (1 mg/mL, 100 μL) were integrated and preincubated in phosphate buffer (pH = 7.4) for 10 min, and then DTNB (3 mg/mL, 66 μL) was added to observe the consumption of GSH. The absorbance at 412 nm was monitored over time. With different concentrations of GSH as the substrate (final concentrations between 0.04 and 0.28 mM), the absorbance at 414 nm was measured over time. The results were fitted using the Michaelis-Menten equation to obtain the Michaelis constant.

4.8 | Cytotoxicity Assay

To assess the cytotoxic effect of MOCs, HK-2 cells were seeded in 96-well plates at 7,000 cells/well and maintained under standard culture conditions (37°C, 12-h incubation). Serial concentrations of MOC solutions (30 and 300 μg/mL, final concentration) were administered to confluent cultures, followed by 24-h exposure. Post-treatment cells underwent three PBS (pH 7.4) rinsing cycles. The Thiazolyl Blue Tetrazolium Bromide (MTT) solution (Beyotime, Shanghai) was added to each well individually and incubated for 4 h in the dark. Subsequently, the cell supernatant was collected using a micropipettor, followed by the addition of 150 μL of DMSO. After thorough agitation for 10 min to completely dissolve MTT crystals, cell viability was assessed using a microplate reader at absorbance wavelengths of 570 nm.

4.9 | Hemolysis Assay

The whole blood of healthy mice was collected in a 2 mL EP tube, and the blood was centrifuged at 2000 rpm for 5 min to remove the upper serum and obtain erythrocytes. Then, erythrocytes were washed three times with PBS, and 0.5 mL of erythrocytes was diluted with 10 mL PBS. Then DDW or MOCs solution (300 μg/mL, final concentration) was added to 0.5 mL erythrocyte suspension. All sample tubes were kept at room temperature for 2 h and then centrifuged at 2000 rpm for 5 min. Finally, the experimental result was recorded by a camera.

4.10 | Cellular Internalization of HEMOC

For in vitro cellular uptake assays, HK-2 cells were inoculated into 10 mm tissue plates at a density of 10,000 cells/mL for 24 h. HEMOC (final concentration 20 μg/mL) was added to each plate and cultured for 0, 4, 8, or 12 h, respectively.

For in vitro cellular retention assays, HK-2 cells were inoculated into 10 mm tissue plates at a density of 10,000 cells/mL for 24 h. HEMOC (final concentration 20 μg/mL) was added to each plate and cultured for 12 h. Then, the medium was extracted, and fresh medium was added. Subsequently, the cells were collected at 2 h (12 + 2 h), 4 h (12 + 4 h), and 6 h (12 + 6 h), respectively.

We used ICP-MS to quantify the cellular uptake of HEMOC. Then the cells were trysinized with trysin, and collected by centrifugation, washed with PBS buffer for 3 times. For traditional ICP-MS analysis, the samples were digested in a solution containing 0.25 mL HNO3 (68%) and 0.75 mL HCl (38%) for 4 h at 110°C. After cooling, the samples were diluted with HCl (2%) to 10 mL. Co contents were then detected by ICP-MS, and calculated the contents of HEMOC according to the HEMOC compositions.

4.11 | Induction of HK-2 Cell Hypoxia/reoxygenation Model

HK-2 cells were maintained in Dulbecco's Modified Eagle Medium/Nutrient Mixture F-12 (DMEM/F12) supplemented with 10% fetal bovine serum and 1% penicillin-streptomycin under standard culture conditions (37°C, 5% CO_2). To establish H/R conditions, cells were exposed to hypoxic parameters (1% O_2, 94% N_2, 5% CO_2) for 24 h at 37°C followed by 6-h reoxygenation under normoxic conditions.

4.12 | In Vitro ROS Determination

The intracellular levels of ROS were assessed using the fluorescent probe DCFH-DA, which reacts with intracellular free radicals to produce dichlorofluorescein (DCF), a fluorescent product. HK-2 cells were seeded in 6-well microplates at a density of 7×10^3 cells per well and maintained under standard culture conditions (37°C, 5% CO_2) for 12 h prior to experimentation. Following medium replacement, MOCs (30 μg/mL, final concentration) were administered to the experimental group, with subsequent incubation for 6 h under identical conditions. After H/R induction, cells underwent DCFH-DA labeling (20 min, 37°C) followed by three successive washes with serum-free medium. Fluorescence intensity measurements were conducted within 1 h using a BD FACS flow cytometer (BD Biosciences, Franklin Lakes, NJ). Complementary fluorescence detection was achieved through confocal microscopy imaging (Nikon A1Si system). For nuclear counterstaining, cells were treated with Hoechst 33342 (10 min) prior to microscopic observation.

4.13 | JC-1 Staining

HK-2 cells were plated in 96-well plates and allowed to adhere overnight under standard culture conditions (37°C, 5% CO_2). Following replacement with serum-free DMEM, cells were exposed to MOCs (30 μg/mL, final concentration) for 6 h. Subsequent to treatment, mitochondrial membrane potential was assessed using the JC-1 fluorescent probe (Beyotime) according to established protocols. Cellular fluorescence was quantitatively analyzed by flow cytometry (BD Biosciences).

4.14 | Animal Experimentation

C57BL/6 mice (7–8 weeks old) were obtained from Shanghai Laboratory Animal Center, China. All animal experiments were performed in accordance with the guidelines of the National Institute of Health for the Care and Use of Laboratory Animals and approved by the Scientific Investigation Committee of Shanghai Jiao Tong University (No. 202501012).

4.15 | Induced Renal Ischemia/Reperfusion Model

Pentobarbital sodium-anesthetized mice (50 mg/kg, intraperitoneal) underwent left renal pedicle occlusion through a retroperitoneal approach. Microvascular clamping (Shanghai Medical Devices, Shanghai) was applied for 30 min, while the contralateral kidney served as a sham control. Temporary wound closure was maintained throughout the ischemic phase. Subsequent clip removal and macroscopic reperfusion verification preceded definitive abdominal wall closure. Core temperature regulation was achieved using a homoeothermic blanket. Postoperative resuscitation included intraperitoneal administration of sterile physiological saline (0.5 mL). Experimental cohorts received MOCs (300 μg/mL, 200 μL) via tail vein injection, with scheduled euthanasia at predetermined reperfusion intervals.

4.16 | Serum Biochemistry Analysis

The mice were sacrificed at the designated time points. All serum samples were collected and subjected to centrifugation at 5000 rpm for 10 min. Serum creatinine levels were quantified using an automated analyzer (Cobas 8000, Roche, Germany) equipped with the c702 module.

4.17 | Histopathological Assessment

Mice were executed at the indicated time points, and mouse kidneys were coronal sectioned, fixed in 10% buffered formalin, paraffin-embedded, and sectioned at a thickness of 3 μm sections were stained with hematoxylin and eosin to assess tissue damage. Kidney sections were blindly labeled and randomized for observation by two researchers. The extent of renal tubular injury was assessed semiquantitatively and pathologically on a scale of 0 to 4: 0 = no recognizable injury; 1 = single cell necrosis; 2 = necrosis of all cells in the adjacent convoluted tubule, with surrounding tubules surviving; 3 = necrosis confined to the distal one-third of the proximal convoluted tubule, with a band of necrosis spanning the endothelial layer; 4 = necrosis affecting all three segments of the proximal convoluted tubule.

4.18 | Immunofluorescence Assay

Kidney frozen sections were processed according to standard protocols. Subsequently, the sections were incubated overnight with anti-DHE, KIM-1, NGAL, or TUNEL primary antibody provided by Beyotime Biotech. After that, the sections were rinsed three times with PBS and then incubated with the secondary antibody for 1 h at room temperature. Nuclear counterstaining was performed with DAPI prior to fluorescence microscopic analysis using a fluorescence microscope (Nikon80i, Tochigi, Japan).

4.19 | Statistical Analysis

Statistical significance was assessed using one-way ANOVA followed by Bonferroni's post hoc test, performed with GraphPad Prism 10 (La Jolla, USA). Data were pre-processed using the Shapiro-Wilk test to evaluate normality; outliers were identified via the Grubbs test and excluded only when technically justified. Analyses were conducted at a significance threshold of $p < 0.05$, with more stringent levels (e.g., $p < 0.01$) reported as appropriate. Data were presented as mean ± standard deviation (SD), and sample sizes (n) were indicated in the corresponding Figure legends.

Author Contributions

D.S. performed data visualization, statistical analysis, and writing. X.F. and Q.M. contributed to sample collection. X.Z. contributed to study design and funding support. J.Y. and Y.W. contributed to the review and revision of the paper.

Acknowledgements

The authors acknowledge the support from the National Key Research and Development Program of China (2022YFC2304700), the Natural Science Foundation of Shanghai (25ZR1403006), and the Fundamental Research Funds for the Central Universities (YG2023QNA04).

Conflicts of Interest

The authors declare no conflicts of interest.

Data Availability Statement

The data that support the findings of this study are available from the corresponding author upon reasonable request.

References

1. J.-W. Yeh, S.-K. Chen, S.-J. Lin, et al., "Nanostructured High-Entropy Alloys With Multiple Principal Elements: Novel Alloy Design Concepts and Outcomes," *Advanced Engineering Materials* 6 (2004): 299–303, https://doi.org/10.1002/adem.200300567.

2. Y. Yao, Q. Dong, A. Brozena, et al., "High-Entropy Nanoparticles: Synthesis-Structure-Property Relationships and Data-Driven Discovery," *Science* 376 (2022): abn3103, https://doi.org/10.1126/science.abn3103.

3. M. Li, F. Lin, S. Zhang, et al., "High-Entropy Alloy Electrocatalysts Go To (Sub-)Nanoscale," *Science Advances* 10 (2024): adn2877, https://doi.org/10.1126/sciadv.adn2877.

4. S. Schweidler, M. Botros, F. Strauss, et al., "High-Entropy Materials for Energy And Electronic Applications," *Nature Reviews Materials* 9 (2024): 266–281, https://doi.org/10.1038/s41578-024-00654-5.

5. L. Han, S. Zhu, Z. Rao, et al., "Multifunctional High-Entropy Materials," *Nature Reviews Materials* 9 (2024): 846–865, https://doi.org/10.1038/s41578-024-00720-y.

6. L. Chang, H. Jing, C. Liu, C. Qiu, and X. Ling, "High-Entropy Materials for Prospective Biomedical Applications: Challenges and Opportunities," *Advanced Science* 11 (2024): 2406521, https://doi.org/10.1002/advs.202406521.

7. Y. Sun and S. Dai, "High-Entropy Materials for Catalysis: A New Frontier," *Science Advances* 7 (2021): abg1600, https://doi.org/10.1126/sciadv.abg1600.

8. A. Laha, S. Yoshida, F. Marques dos Santos Vieira, et al., "High-Entropy Engineering of the Crystal And Electronic Structures In A Dirac Material," *Nature Communications* 15 (2024): 3532, https://doi.org/10.1038/s41467-024-47781-9.

9. W.-L. Hsu, C.-W. Tsai, A.-C. Yeh, and J.-W. Yeh, "Clarifying The Four Core Effects Of High-Entropy Materials," *Nature Reviews Chemistry* 8 (2024): 471–485, https://doi.org/10.1038/s41570-024-00602-5.

10. Q. Ding, Y. Zhang, and X. Chen, et al., "Tuning Element Distribution, Structure And Properties by Composition in High-Entropy Alloys," *Nature* 574 (2019): 223–227, https://doi.org/10.1038/s41586-019-1617-1.

11. S. Divilov, H. Eckert, D. Hicks, et al., "Disordered Enthalpy–Entropy Descriptor for High-Entropy Ceramics Discovery," *Nature* 625 (2024): 66–73, https://doi.org/10.1038/s41586-023-06786-y.

12. F. Otto, Y. Yang, H. Bei, and E. P. George, "Relative Effects Of Enthalpy And Entropy on The Phase Stability Of Equiatomic High-Entropy Alloys," *Acta Materialia* 61 (2013): 2628–2638, https://doi.org/10.1016/j.actamat.2013.01.042.

13. X. Chang, M. Zeng, K. Liu, and L. Fu, "Phase Engineering of High-Entropy Alloys," *Advanced Materials* 32 (2020): 1907226, https://doi.org/10.1002/adma.201907226.

14. Y. Yao, Z. Huang, P. Xie, et al., "Carbothermal Shock Synthesis Of High-Entropy-Alloy Nanoparticles," *Science* 359 (2018): 1489–1494, https://doi.org/10.1126/science.aan5412.

15. B. Wang, C. Wang, X. Yu, et al., "General Synthesis Of High-Entropy Alloy And Ceramic Nanoparticles in Nanoseconds," *Nature Synthesis* 1 (2022): 138–146, https://doi.org/10.1038/s44160-021-00004-1.

16. X. Sun and Y. Sun, "Synthesis Of Metallic High-Entropy Alloy Nanoparticles," *Chemical Society Reviews* 53 (2024): 4400–4433, https://doi.org/10.1039/D3CS00954H.

17. Z. Lei, X. Liu, Y. Wu, et al., "Enhanced Strength And Ductility in a High-Entropy Alloy via Ordered Oxygen Complexes," *Nature* 563 (2018): 546–550, https://doi.org/10.1038/s41586-018-0685-y.

18. R. Feng, C. Zhang, M. C. Gao, et al., "High-Throughput Design Of High-Performance Lightweight High-Entropy Alloys," *Nature Communications* 12 (2021): 4329, https://doi.org/10.1038/s41467-021-24523-9.

19. Y. Sohail, C. Zhang, D. Xue, et al., "Machine-Learning Design of Ductile FeNiCoAlTa Alloys With High Strength," *Nature* 643 (2025): 119–124, https://doi.org/10.1038/s41586-025-09160-2.

20. J. Hu, T. Guo, X. Zhong, et al., "Situ Reconstruction of High-Entropy Heterostructure Catalysts for Stable Oxygen Evolution Electrocatalysis Under Industrial Conditions," *Advanced Materials* 36 (2024): 2310918, https://doi.org/10.1002/adma.202310918.

21. S. Moniri, Y. Yang, J. Ding, et al., "Three-Dimensional Atomic Structure And Local Chemical Order Of Medium- And High-Entropy Nanoalloys," *Nature* 624 (2023): 564–569, https://doi.org/10.1038/s41586-023-06785-z.

22. D. Nam, J. Kim, E. Hwang, et al., "Multivariate Porous Platform Based on Metal-Organic Polyhedra With Controllable Functionality Assembly," *Matter* 4 (2021): 2460–2473, https://doi.org/10.1016/j.matt.2021.04.027.

23. W. Jiang, C.-C. Liang, and Y.-B. Zhang, "Multivariate Metal–Organic Frameworks for Programming Functions," *Advanced Functional Materials* 34 (2024): 2308946, https://doi.org/10.1002/adfm.202308946.

24. J. Xing, Y. Liu, G. Mathew, et al., "High-Entropy Metal–Organic Frameworks and Their Derivatives: Advances in Design, Synthesis, and Applications for Catalysis and Energy Storage," *Advanced Science* 12 (2025): 2411175, https://doi.org/10.1002/advs.202411175.

25. A. J. Gosselin, C. A. Rowland, and E. D. Bloch, "Permanently Microporous Metal–Organic Polyhedra," *Chemical Reviews* 120 (2020): 8987–9014, https://doi.org/10.1021/acs.chemrev.9b00803.

26. J. Liu, Z. Wang, P. Cheng, M. J. Zaworotko, Y. Chen, and Z. Zhang, "Post-Synthetic Modifications Of Metal–Organic Cages," *Nature Reviews Chemistry* 6 (2022): 339–356, https://doi.org/10.1038/s41570-022-00380-y.

27. D. Sun, X. Feng, X. Zhu, Y. Wang, and J. Yang, "Anticancer Agents Based on Metal Organic Cages," *Coordination Chemistry Reviews* 500 (2024): 215546, https://doi.org/10.1016/j.ccr.2023.215546.

28. D. Zhang, T. K. Ronson, Y.-Q. Zou, and J. R. Nitschke, "Metal–Organic Cages for Molecular Separations," *Nature Reviews Chemistry* 5 (2021): 168–182, https://doi.org/10.1038/s41570-020-00246-1.

29. K.-K. Liu, Z.-J. Guan, M. Ke, and Y. Fang, "Bridging the Gap Between Charge Storage Site and Transportation Pathway in Molecular-Cage-Based Flexible Electrodes," *ACS Central Science* 9 (2023): 805–815, https://doi.org/10.1021/acscentsci.3c00027.

30. P. Yin, D. Sun, Y. Deng, et al., "Metal-Organic Cage As A Theranostic Nanoplatform for Magnetic Resonance Imaging Guided Chemodynamic Therapy," *Theranostics* 14 (2024): 4861–4873, https://doi.org/10.7150/thno.97264.

31. D. Sun, Y. Deng, J. Dong, X. Zhu, J. Yang, and Y. Wang, "Heterometallic Organic Cages As Cascade Antioxidant Nanozymes To Alleviate Renal Ischemia-Reperfusion Injury," *Chemical Engineering Journal* 497 (2024): 154648, https://doi.org/10.1016/j.cej.2024.154648.

32. L. K. Moree, L. A. V. Faulkner, and J. D. Crowley, "Heterometallic cages: Synthesis and applications," *Chemical Society Reviews* 53 (2024): 25–46, https://doi.org/10.1039/D3CS00690E.

33. B. Chang, L. Zhang, S. Wu, Z. Sun, and Z. Cheng, "Engineering Single-Atom Catalysts Toward Biomedical Applications," *Chemical Society Reviews* 51 (2022): 3688–3734, https://doi.org/10.1039/D1CS00421B.

34. Z. Guo, J. Hong, N. Song, and M. Liang, "Single-Atom Nanozymes: From Precisely Engineering to Extensive Applications," *Accounts of Materials Research* 5 (2024): 347–357, https://doi.org/10.1021/accountsmr.3c00250.

35. Y. Liu, H. Zhao, and Y. Zhao, "Designing Efficient Single Metal Atom Biocatalysts at the Atomic Structure Level," *Angewandte Chemie International Edition* 63 (2024): 202315933, https://doi.org/10.1002/anie.202315933.

36. J. Shen, J. Chen, Y. Qian, et al., "Atomic Engineering of Single-Atom Nanozymes for Biomedical Applications," *Advanced Materials* 36 (2024): 2313406, https://doi.org/10.1002/adma.202313406.

37. M. R. Dworzak, *Synthesis, Modification, and Utilization of Calixarene-Capped Coordination Cages* (University of Delaware, 2023).

38. B. Jiang, D. Duan, L. Gao, et al., "Standardized Assays for Determining The Catalytic Activity And Kinetics Of Peroxidase-Like Nanozymes," *Nature Protocols* 13 (2018): 1506–1520, https://doi.org/10.1038/s41596-018-0001-1.

39. Y. Liu, Y. Cheng, H. Zhang, et al., "Integrated Cascade Nanozyme Catalyzes in Vivo ROS Scavenging for Anti-Inflammatory Therapy," *Science Advances* 6 (2020): abb2695, https://doi.org/10.1126/sciadv.abb2695.

40. Q. Miao, H. Yang, X. Zhu, X. Feng, J. Yang, and Y. Wang, "Cascade Nanozymes as ROS Scavengers for The Treatment Of Aseptic Inflammation," *Coordination Chemistry Reviews* 548 (2026): 217163, https://doi.org/10.1016/j.ccr.2025.217163.

41. S. Marchi, E. Guilbaud, S. W. G. Tait, T. Yamazaki, and L. Galluzzi, "Mitochondrial Control Of Inflammation," *Nature Reviews Immunology* 23 (2023): 159–173, https://doi.org/10.1038/s41577-022-00760-x.

42. F. Sivandzade, A. Bhalerao, and L. Cucullo, "Analysis of the Mitochondrial Membrane Potential Using the Cationic JC-1 Dye as a Sensitive Fluorescent Probe," *Bio-protocol* 9 (2019): 3128, https://doi.org/10.21769/BioProtoc.3128.

Supporting Information

Additional supporting information can be found online in the Supporting Information section.

Supporting File: adhm70642-sup-0001-SuppMat.docx.